PHYSICAL REVIEW A **106**, 043507 (2022)

Counterpropagating light in ring resonators: Switching fronts, plateaus, and oscillations

Graeme N. Campbell,[1,*] Shuangyou Zhang,[2] Leonardo Del Bino,[2,3] Pascal Del'Haye,[2,3] and Gian-Luca Oppo[1]
[1]*SUPA and Department of Physics, University of Strathclyde, Glasgow, G4 0NG, Scotland, United Kingdom*
[2]*Max Planck Institute for the Science of Light, 91058 Erlangen, Germany*
[3]*Department of Physics, Friedrich Alexander University Erlangen-Nuremberg, 91058 Erlangen, Germany*

(Received 1 April 2022; revised 15 September 2022; accepted 19 September 2022; published 10 October 2022)

We characterize the formation of robust stationary states formed by light plateaus separated by two local switching fronts in only one of two counterpropagating fields in ring resonators with normal dispersion. Such states are due to global cross coupling and allow for frequency combs to switch from one field to the other by simply tuning the input laser frequency. Exact expressions for the distance between fronts and for plateau powers are provided in excellent agreement with simulations. These demonstrate an unusual high degree of control over pulse and plateau duration in one of the fields upon changes of one of the input laser frequencies. We identify a wide parameter region in which light plateaus are self-starting and are the only stable solution. For certain values of the detunings we find multistable states of plateaus with switching fronts, slowly oscillating homogeneous states and nonoscillating homogeneous states of the counterpropagating fields. Robustness and multistability of these unusual single-field front solutions are provided in parameter ranges that are experimentally achievable in a wide variety of ring resonators.

DOI: 10.1103/PhysRevA.106.043507

I. INTRODUCTION

The physics of microring resonators has gained significant interest over the last decade for their many applications such as octave spanning frequency combs [1] for use in telecommunication [2,3] and spectroscopy [4,5], as well as fundamental studies of dissipative pattern formation and temporal cavity solitons (TCS) [6]. The microring resonator system is well described by the longitudinal version of the Lugiato-Lefever equation (LLE) [7] in the form of a damped, driven nonlinear Schrödinger equation with cavity detuning. It originally described the transverse, dissipative spatial structures in passive optical systems with diffraction and was later adapted into a longitudinal form to describe temporal pattern formation along the cavity length [8,9].

In this paper we study the interaction of two counterpropagating input fields in normally dispersive ring and microring resonators, which is described by two globally coupled equations of LLE form [10,11]. We use the term "global coupling" following [12] to describe nonlinear cross terms that couple a point of the resonator to all other points in the same resonator via integrals that extend to its full length. The anomalous dispersion case has been investigated in [13] where the soliton blockade phenomenon was introduced. We characterize the formation of a different class of robust stationary states formed by light plateaus separated by two local switching fronts in only one of two counterpropagating fields in ring resonators. Such states are due to global coupling between counterpropagating fields corresponding to the average power, and allow for frequency combs to switch from one field to the other by simply tuning the input laser frequency. Light plateau states are self-starting from noise for a wide range of detuning due to a spatial instability of the homogeneous stationary states resulting from the averaged terms. The global nature of these states display an unusual high degree of control over pulse and plateau duration in one of the fields upon changes of one of the input laser frequencies.

In Sec. II homogeneous steady-state solutions of the globally coupled cavity field equations of both fields are investigated and shown to undergo several bifurcations when the detunings are scanned. In Sec. III we characterize steady-state solutions where one field has a homogeneous power while the other forms either a single dark TCS, a single bright TCS, or power plateaus separated by sharp kinks. These solutions are unusual because in coupled field equations fast time variations of the power of one field are reflected in the other one. It is the nature of the integro-partial-differential equations and global coupling that variations in one field are not present in the other one leaving it in a homogeneous state. In Sec. IV we determine the parameter ranges of the existence and stability of these hybrid solutions with sharp kinks, derive a semianalytical expression of the distance of stationary kinks as a function of the cavity detunings and compare it successfully with numerical simulations. In particular we demonstrate that stationary solutions with two kinks in one of the counterpropagating fields are strongly related to similar solutions in a single normally dispersive LLE at the Maxwell point. Such stationary states have been observed with single-input laser setups where a counterpropagating field is induced by backscattering [14,15], where a connection with the Maxwell point (see Sec. III) is also made.

Steep kinks connecting two stable homogeneous solutions in the presence of bistability have been studied extensively

---

[*] graeme.campbell.2019@uni.strath.ac.uk

in diffusive systems where they are known as fronts [16], in nonlinear optics of scalar fields where they are known as switching waves [17–19], and in systems with exchange symmetry where they are known as domain walls [20–24]. The system of interest here has exchange symmetry between the two counterpropagating fields. The hybrid solutions described in Sec. III display power plateaus separated by two kinks and do not reflect this exchange symmetry since one field is homogeneous and the other one is not. For this reason we prefer to label the kinks as "switching fronts" (SFs) instead of "domain walls" which was preferred in for example [15]. The solitonic (localized) aspect of these solutions is located in the SF and not of course in the power plateaus. For this reason we also avoid the use of the term "platicons" as being an unhelpful mixing of the localized aspect of solitons with the extended character of the homogeneous solutions. In Sec. V we derive a semianalytical description of zero dispersion SFs, and show that the zero dispersion SF solutions well approximate transient states with nonzero dispersion as they move towards stable two-SF states. In Sec. VI we show the presence of nonlinear oscillations of homogeneous states in a symmetry broken and global regime similar to those predicted in symmetric regimes [25,26]. We then identify a multistability of slow nonlinear oscillations with SF states and continuous wave outputs offering an unprecedented variety of states for applications in high-control frequency comb generation, all optical oscillators, optical computing, time reversal symmetry breaking, and signal routing in telecommunication systems. Conclusions, connection to experiments, and applications are presented in Sec. VII.

II. COUNTERPROPAGATION IN RING RESONATORS

We consider the physical setting of a ring resonator pumped with two counterpropagating continuous wave (CW) lasers (see Fig. 1). The two fields of this system are described by mean-field equations with the self- and cross-coupling terms in the Kerr approximation, through which the fields interact. The phase dynamics of the cross-coupling terms evolve with the free spectral range by the nature of counterpropagation of the two fields. This results in a large walk-off occurring between the two counterpropagating waves that see each other through an average intensity (washout effect) [10,11]. The model for this system can be written in the adimensional, normalized form as a system of two integro-partial-differential equations

$$\partial_t F = E_F - (1 + i\theta_F)F + i(|F|^2 + \nu\langle|B|^2\rangle)F - i\beta\partial_\zeta^2 F, \tag{1}$$

$$\partial_t B = E_B - (1 + i\theta_B)B + i(|B|^2 + \nu\langle|F|^2\rangle)B - i\beta\partial_\zeta^2 B, \tag{2}$$

where we define "slow time" $t = \alpha\tilde{t}/t_\mathrm{R}$, which governs evolution over several round trips of the resonator with round trip time t_R, and "fast time" $\zeta = \tilde{\zeta}\sqrt{2\alpha/L}$ corresponding to the cavity coordinate with cavity length L in a frame of reference moving with the group velocity. $F = \tilde{F}\sqrt{\gamma L/\alpha}$ and $B = \tilde{B}\sqrt{\gamma L/\alpha}$ are the complex amplitudes of the forward and backward counterpropagating fields in the ring resonator with identical polarization, with input fields $E_F = \tilde{E}_F\sqrt{\gamma LT/\alpha^3}$ and $E_B = \tilde{E}_B\sqrt{\gamma LT/\alpha^3}$ for nonlinear coefficient γ, power

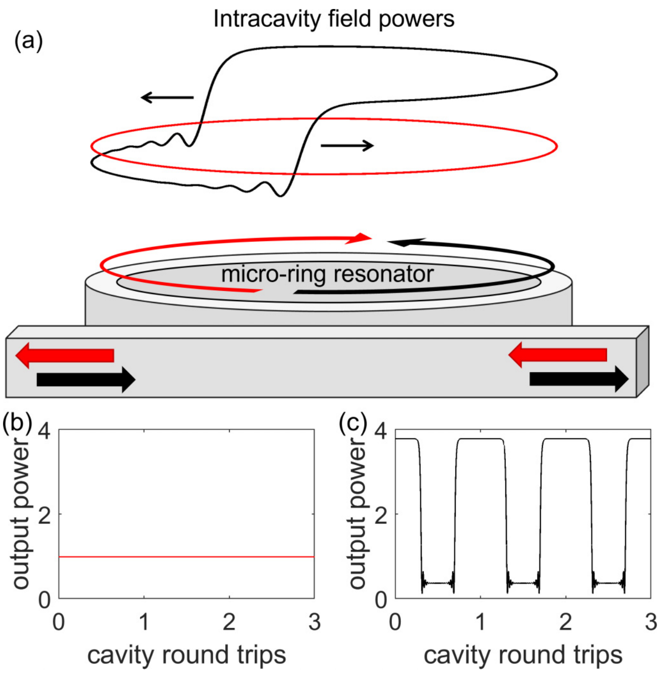

FIG. 1. A continuous wave (CW) forward (red) and a CW backward (black) beams counterpropagate in a microring resonator. For a detuning of the forward field smaller than the detuning of the backward field it is possible to obtain a power output where the forward field is still CW while the backward field displays two SFs in the intracavity power (a). This results in a switching output (c) from the backward field and CW output (b) from the forward field.

transmission coefficient T, and total losses α. $\theta_F = t_\mathrm{R}(\omega_\mathrm{r} - \omega_F)/\alpha$ and $\theta_B = t_\mathrm{R}(\omega_\mathrm{r} - \omega_B)/\alpha$ are the laser detunings of angular frequency ω_F, ω_B from the nearest cavity resonance ω_r with round trip time t_R. ν is the cross-coupling coefficient that is in general equal to 2 for isotropic media, and the last term describes normal dispersion with a positive dispersion coefficient β. We define the power averages $\langle|F|^2\rangle$ and $\langle|B|^2\rangle$ as

$$\langle|F|^2\rangle = \frac{1}{L}\int_0^L |F|^2\, d\zeta, \tag{3}$$

$$\langle|B|^2\rangle = \frac{1}{L}\int_0^L |B|^2\, d\zeta. \tag{4}$$

The configuration and parameters used here differ from those used in [14,15] in that we consider energy injection on both fields. It is important to note that for $E_F = E_B$ and $\theta_F = \theta_B$ the system is perfectly symmetric upon the exchange of the forward and backward fields.

Homogeneous steady states

The homogeneous steady-state solutions (HSSs) of counterpropagating fields are identical to the two polarization copropagating regimes seen in [25,27] due to the cross terms containing $\langle|F|^2\rangle = |F|^2$, $\langle|B|^2\rangle = |B|^2$. Equations (1) and (2) can be expressed by the coupled cubic equations

$$P_F = H_F^3 - 2(\theta_F - \nu H_B)H_F^2 + ((\theta_F - \nu H_B)^2 + 1)H_F, \tag{5}$$

$$P_B = H_B^3 - 2(\theta_B - \nu H_F)H_B^2 + ((\theta_B - \nu H_F)^2 + 1)H_B, \tag{6}$$

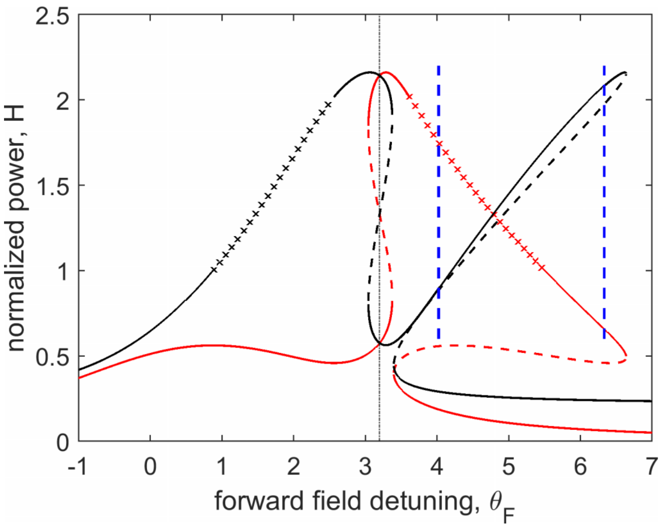

FIG. 2. Powers H_F (red) and H_B (black) of HSS (5,6) when changing the detuning θ_F of the forward field for parameter values $E_F = E_B = 1.47$, $\nu = 2$, and the detuning of the backwards field kept constant at $\theta_B = 3.2$. The solid (dashed) lines correspond to stable (unstable) HSS, the lines marked with the symbol X correspond to HSS unstable to fast time perturbations, the vertical blue dashed lines correspond to Hopf bifurcations of the HSS.

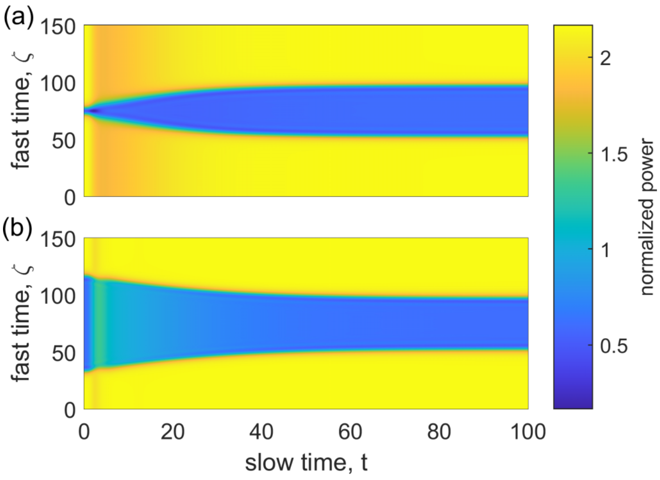

FIG. 3. Temporal evolution of the backward power towards a stable SF state for $|E_F|^2 = |E_B|^2 = 2.1609$, $\theta_F = 2.0$, $\theta_B = 3.2$ from two different initial conditions with dispersion $\beta = 1$. (a) Initial condition with two kinks at narrow separation. (b) Initial condition with two kinks at wide separation.

where $H_F = |F|^2$, $H_B = |B|^2$ (the letter H referring to the power of the HSS) while $P_F = |E_F|^2$ and $P_B = |E_B|^2$ correspond to the input powers. Counterpropagating fields in ring resonators display spontaneous symmetry breaking of the HSS for equal detunings. This allows for optical switching between high- and low-power counterpropagating fields, which has been observed experimentally [28,29]. For our purposes, we consider different detunings.

These algebraic equations can be solved numerically for given values of the parameters, an example of which is shown in Fig. 2 for $\nu = 2$, equal pump powers ($P_F = P_B = 2.1609$) with one of the field detuning kept constant ($\theta_B = 3.2$) while the other (θ_F) is changed. In the vicinity of equal detunings (dot dashed line) where the equations are symmetric upon exchange of the forward and backward fields, a bistability regime with a “Figure 8” shape exists. Here we expect the “middle” HSS to be unstable (see dashed lines in Fig. 2). When increasing the forward detuning θ_F after the symmetric value 3.2, the Figure 8 ends in this case at the point where two new HSS are born in a degenerate saddle-node bifurcation, the lowermost being stable and the intermediate unstable. For values of $\theta_B < 3.2$ the saddle-node bifurcation takes place after the end of the Figure 8, while for values of $\theta_B > 3.2$ the saddle-node bifurcation takes place before the end of the Figure 8 leading to a simultaneous presence of five different stationary states. After the saddle-node bifurcation and the end of the Figure 8, multistability of homogeneous solutions is present at large values of the detuning θ_F until a reverse saddle-node bifurcation restores a single HSS at very large values of the scanned detuning.

In the asymmetric region for $\theta_F > \theta_B$ we detect Hopf bifurcations of the HSS leading to oscillations as described in Sec. VI. The two Hopf bifurcations occur on the upper branches of the HSS (see the vertical dashed lines in Fig. 2) and have opposite directions when increasing the detuning θ_F, with the amplitude of the oscillation growing from around $\theta_F = 4$ and decreasing to zero around $\theta_F = 6.3$. These forward and backward Hopf bifurcations are analogous in nature and stability eigenvalues to those described in [25,27] where, however, the two detunings where kept equal to each other during the scan to focus on symmetric HSS.

There are however further instabilities of the HSS due to the nature of the global coupling of Eqs. (1) and (2). In Appendix A, a linear stability analysis of the HSS to inhomogeneous perturbations at zero dispersion on the fast time scale is presented. A new set of stability eigenvalues is found:

$$\lambda = -1 \pm \sqrt{-A_1 B_1}, \tag{7}$$

$$\lambda = -1 \pm \sqrt{-A_2 B_2}, \tag{8}$$

where $A_1 = H_F + \nu H_B - \theta_F$, $A_2 = H_B + \nu H_F - \theta_B$, $B_1 = 3H_F + \nu H_B - \theta_F$, $B_2 = 3H_B + \nu H_F - \theta_B$, with H_F and H_B being obtained from Eqs. (5) and (6). These new eigenvalues are entirely due to the averaged terms of this system which means that local perturbations result in changes to the unperturbed regions. The lines marked with the letter X in Fig. 2 correspond to the HSS instability to inhomogeneous perturbations where the real part of at least one of the four eigenvalues (8) is positive.

III. TWO SWITCHING FRONTS AND DARK SOLITON STEADY STATES

In the counterpropagating system with global coupling described by Eqs. (1) and (2), we observe the formation of steady states made of power plateaus separated by SFs in one of the two counterpropagating fields while the second field remains homogeneous, for wide ranges of the detuning values. In Fig. 3 we show the formation of stable SF states when starting

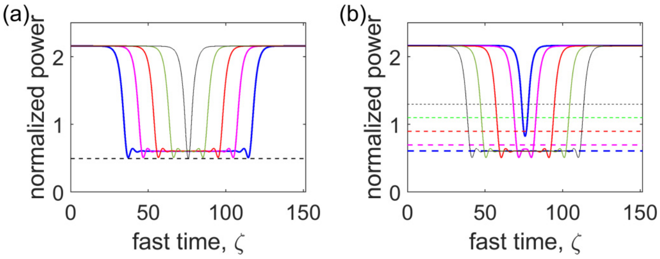

FIG. 4. Various SF states for $E_F = E_B = 1.47$, $\nu = 2$, $\beta = 1$, $\theta_B = 3.2$. (a) Backward (forward) field power of steady-state solutions, solid lines (dashed lines), for five values with decreasing distance between SFs $\theta_F = 1.2$ (blue), $\theta_F = 1.6$ (magenta), $\theta_F = 2.0$ (red), $\theta_F = 2.4$ (green), $\theta_F = 2.8$ (black). (b) Forward (backward) field power of steady-state solutions, solid lines (dashed lines) for five values with increasing distance between SFs $\theta_F = 3.4$ (blue), $\theta_F = 3.6$ (magenta), $\theta_F = 4.0$ (red), $\theta_F = 4.4$ (green), $\theta_F = 4.8$ (black).

from a narrow [Fig. 3(a)] or broad [Fig. 3(b)] perturbation of the HSS for $E_F = E_B = 1.47$, $\nu = 2$, $\theta_B = 3.2$, and $\theta_F = 2.0$. We note that the choice of input power was arbitrary, and similar solutions of stable SFs will exist for input field with similar values, such as $E_F = E_B = 1.5$ or $E_F = E_B = \sqrt{2}$. In Sec. II A we showed that in this parameter region, HSS are unstable to inhomogeneous perturbations. In both cases of broad and narrow initial perturbations, the system evolves to the same final state formed by a SF state with a well-defined separation of the two SFs. It is important to note that the SF solutions do not connect HSS of Eqs. (1) and (2) and affect only one of the counterpropagating fields, the other being homogeneous. They do not correspond to symmetry exchanges of the F and B fields.

A number of stable asymptotic states are presented in Fig. 4 for the same values of the parameters as Fig. 3 but with θ_F varying from 1.2 to 4.8. In the interval $1.2 < \theta_F < 2.8$ the backward (forward) intracavity power is nonhomogeneous (homogeneous) [Fig. 4(a)], while in the interval $3.4 < \theta_F < 4.8$ the forward (backward) intracavity power is nonhomogeneous (homogeneous) [Fig. 4(b)]. The solid lines correspond to the power profiles of the field where a dark structure is found while the dashed lines correspond to fully homogeneous solutions. When the two detunings are close to each other (for example, θ_F equal to 2.8 or 3.4 in Fig. 4) the inhomogeneous field has the shape of a localized dark soliton. In the interval of $2.8 < \theta_F < 3.4$, there are no inhomogeneous stable solutions and the system relaxes to the HSS seen in Fig. 2. This instability of the dark soliton solution is affected by the dispersion of the field, and dark solitons can persist in larger detuning ranges for $\beta < 1$. For the present choice of parameter values there is no bistability between the two-SF states close to detuning symmetry. We will see in Sec. IV that for $P_F = P_B = 3$, for example, an overlap region where both SF states are stable, exists. In this overlap region, bistability of SF states is observed where SFs are present in either the forward or the backward field with the other field homogeneous for the same parameter values.

For detunings $\theta_F < \theta_B$ below symmetry, there is a wide region of parameter space where SFs separated by light plateaus are the only stable solutions of the system. Here light plateaus within two SFs are self-starting states and there is no need of any perturbation to the system to drive the dynamics towards them.

For $\theta_F < \theta_B$ there are small regions of bistability between HSS and light plateaus within two SFs. For $\theta_F > \theta_B$ there is a wide region of bistability between low-intensity HSS and light plateaus within two SFs and even tristability with the addition of oscillating HSS. In all the regions of multistability we have found that input pulses made of a square wave of around twice the background input power, of duration $\tilde{\zeta}$ and applied for a transient time $\tilde{t}$ to the field where the light plateaus will appear results in the formation of stationary light plateaus within two SFs if the input pump pulse duration $\tilde{\zeta}/L$ is of the order of $(1-\Delta)$ where Δ is the final separation of the SFs (see Sec. IV).

When the two detunings are very different from each other, the inhomogeneous field can take the shape of a localized bright soliton while the other field remains homogeneous. Bright solitons are in general not stable in the normally dispersive unidirectional system (LLE) and annihilate each other as the fronts collide. Bright solitons formed by two SFs are instead stable in counterpropagation due to the robustness introduced by global coupling but the SFs will still annihilate if brought too close to each other. Such states have been observed in single laser setups [14]. In the limit of zero dispersion, bright structures can be made arbitrarily narrow when changing the detuning. The dispersion affects the steepness of SFs and for a given θ_F, it will determine whether we have a bright structure of two non interacting SFs or a bright soliton or an annihilation of the two SFs. For given values of the detunings, bright structures with a minimum full width at half maximum (FWHM) can be found and their dependence from the dispersion coefficient β can be established in numerical simulations as shown in Fig. 5. Stable SF states and stable dark solitons are present due to the global coupling of the two counterpropagating fields. The phase-independent interaction of counterpropagating fields introduced a shift in the detuning of the fields. To this end we define effective detunings

$$\tilde{\theta}_F = \theta_F - \nu\langle|B|^2\rangle, \tag{9}$$

$$\tilde{\theta}_B = \theta_B - \nu\langle|F|^2\rangle \tag{10}$$

that reduce the counterpropagating Eqs. (1) and (2) to a pair of LLEs coupled via their effective detunings:

$$\partial_t F = E_F - (1 + i\tilde{\theta}_F)F + i|F|^2F - i\beta\partial_\zeta^2 F, \tag{11}$$

$$\partial_t B = E_B - (1 + i\tilde{\theta}_B)B + i|B|^2B - i\beta\partial_\zeta^2 B. \tag{12}$$

Taken separately when ignoring the coupling through the effective detunings, each of these LLEs displays a Maxwell point for normal dispersion corresponding to a set of parameter values where solutions made of power plateaus well separated by SFs are stable. For any other parameter value close to the Maxwell point, SFs are observed to move close or away from each other. At the Maxwell point and at the Maxwell point only, the LLE displays a multistability of power plateaus solutions with two stationary SFs at

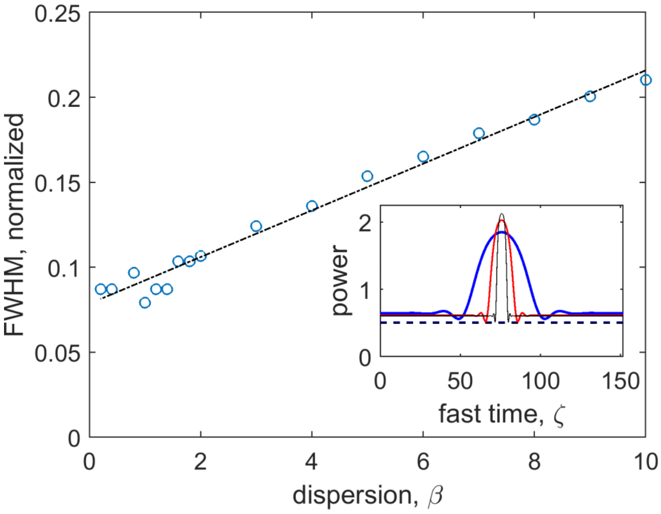

FIG. 5. Minimum possible FWHM size of bright solitons for different values of the dispersion coefficient β at parameter values $P_F = P_B = 2.1609$, $\theta_B = 3.2$ where θ_F is chosen to provide the narrowest soliton for each value of β. Circles represent the FWHM values from simulations while the dashed line is a linear fit of the data. Inset: Power distribution of three bright solitons of minimum FWHM in the backward field while the forward power remains constant (dashed line) for dispersion values $\beta = 0.1$ (black line), $\beta = 1$ (red line), and $\beta = 10$ (blue line) with increasing FWHM.

arbitrary separations. In gradient systems the Maxwell point corresponds to the parameter value where both bistable homogeneous states have equal energy. In nongradient system, such as the LLE, Maxwell points and hysteresis can still be possible even though an expression of the energy cannot be obtained.

There are very important differences between our SF states and dark solitons due to global coupling and structures of similar shape in the single LLE with normal dispersion (at the Maxwell point or close to the Maxwell point) studied theoretically in [18,30] and experimentally in [19,31,32]. For example, the power of the homogeneous field and the power values of the plateaus before and after the two SFs in the inhomogeneous field are not the values of the HSS studied in Sec. II A. When the values of the two field detunings are well separated, stable SF states are not due to locking mechanisms of the tails of the SFs as for example observed in optical parametric oscillators [21,22]. However, when the detunings of the two fields are quite close to each other, dark solitons owe their stability to the local oscillations in the lower part of the SF as shown in Fig. 4 for $\theta_B = 3.2$ and $\theta_F = 2.8$, 3.4 and 3.6.

When increasing the detuning θ_F while keeping the detuning θ_B fixed, one observes first a decreasing separation between the two stable SFs in the backward field [Fig. 4(a)] and then, after the symmetric state $\theta_F = \theta_B$, an increasing distance between the two stable SFs in the forward field as seen in Fig. 4(b). In the latter case, the power of the homogeneous backward field changes substantially upon variations of $\theta_F > \theta_B$ while the power of the homogeneous forward field changes only a little upon variations of $\theta_F < \theta_B$ [see Fig. 4(a)]. This effect is a direct result of the effective detunings that contain the integrals (4).

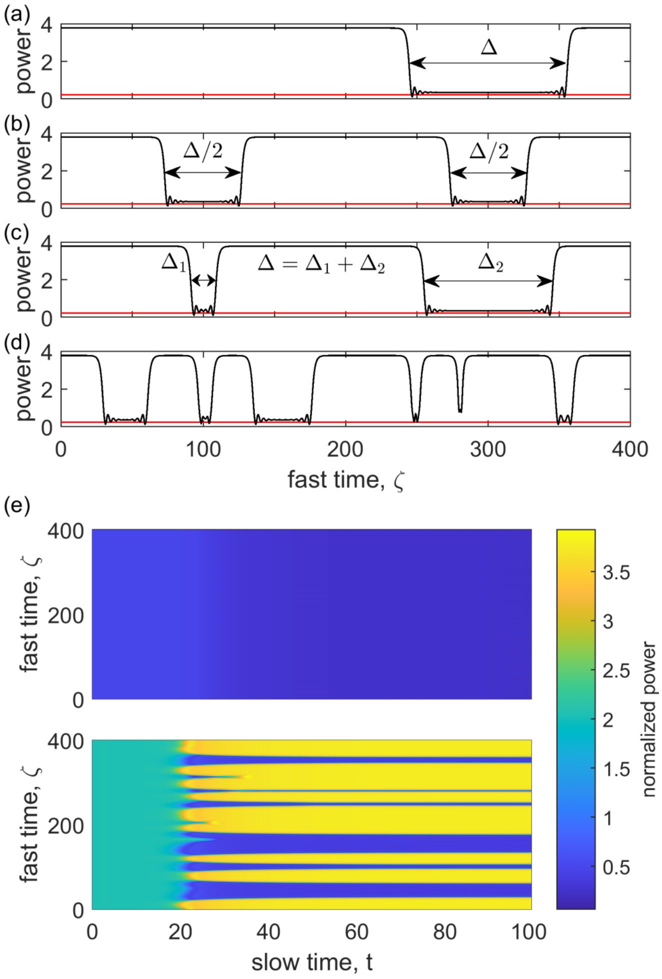

FIG. 6. (a–d). Light plateau stationary solutions obtained from different perturbations of the HSS, displaying either two SFs (a) or four SFs (b–c), or dark solitons and SFs (d) for $P_F = P_B = 4$, $\theta_B = 4$ and $\theta_F = 1.9$ ($\Delta \approx 0.3$). A single wide perturbation gives a two-SF stationary state (a); two perturbations of equal (b) or unequal width (c) give four SF stationary states. (d) A stationary state resulting from the spontaneous formation of SFs and dark structures due to small amplitude initial noise. In each case (a–d) the average power of the field and the plateau powers are identical. (e) Evolution to a stationary state with SFs and dark solitons in the backward field (lower) with flat forward field (upper) due to noise. The final stationary state is shown in (d).

One very interesting feature when scanning one of the detunings (say, θ_F) while keeping the other one fixed by changing the input frequency of one of the two pumps, is that upon crossing the symmetric state $\theta_F = \theta_B$, stable SFs and dark solitons switch from one propagation direction (the backward for $\theta_F < \theta_B$) to the other (the forward for $\theta_F > \theta_B$). This provides the operator of this device to select at will the direction, in which the solitary structures and, consequently, an optical frequency comb occurs.

In general $2N$ SFs may coexist within a long cavity. Two examples of stationary states with four SFs are shown in Figs. 6(b) and 6(c). At stationary state, the upper and lower power plateaus connected by the four SFs have identical power to the plateaus of the two-SF stationary state shown in Fig. 6(a). The average power of a $2N$ SF stationary state is also identical to the two-SF stationary state. This is due to the Maxwell point condition on the effective detuning. As such the total proportion of the upper and lower plateaus for all $2N$ SF stationary states are identical. This means that the distance between SFs of each pair $\Delta_1, \dots, \Delta_N$ of $2N$ SFs sums up to the SF distance Δ of the two-SF stationary state, $\Delta = \sum_{n=1}^{N} \Delta_n$. In regions of the spatial instability of the HSS, different SF structures may form. Figures 6(d) and 6(e) shows the spontaneous formation of many SFs from an unstable HSS under the action of noise. The location and separations of SFs of the stationary state [Fig. 6(d)] are random, showing plateaus and dark soliton structures coexisting in the cavity, and yet satisfying the constraint on the sum of Δ_n being Δ.

IV. DISTANCE OF TWO STATIONARY SWITCHING FRONTS

From numerical simulations we obtain stationary solutions with two stable SFs separated by a distance Δ. We aim here to obtain an analytical expression of the the distance Δ when using θ_F as a control parameter.

We start from the case of two SFs in the backward field for a given value of θ_B when changing $\theta_F < \theta_B$ [see Fig. 4(a)]. In this case the forward field power $|F|^2$ is homogeneous and appears to be independent of the detuning θ_F. Note that this homogeneous value of the forward power is not the HSS value H_F discussed in Sec. III. For the stationary solutions we can write

$$E_F = (1 + i\tilde{\theta}_F)F - i|F|^2F, \tag{13}$$

$$E_B = (1 + i\tilde{\theta}_B)B - i|B|^2B + i\beta\partial_\zeta^2 B, \tag{14}$$

where we have used Eqs. (9) and (10). Each solution of the backward field equation (14) when changing θ_F has a one-to-one correspondence with one of the multistable stationary solutions of a single Lugiato-Lefever equation (LLE) at the Maxwell point given by

$$E_B = (1 + i\Theta_{\text{MP}})B - i|B|^2B + i\beta\partial_\zeta^2 B, \tag{15}$$

where Θ_{MP} is the cavity detuning at Maxwell point which depends on the input power P_B. The functional dependence of Θ_{MP} from P_B can be obtained by asymptotic methods close to the critical detuning value $\sqrt{3}$ for $P_B \approx 8\sqrt{3}/9$ and by variational methods for $P_B > 10$ [15]. Neither of these approximations is satisfactory in the range $2 < P_B < 7$ of values used here (see Fig. 7). By computing the Maxwell points numerically (see blue line in Fig. 7) we find that a simple linear dependence of Θ_{MP} from P_B

$$\Theta_{\text{MP}} \approx \eta(1 + P_B) \tag{16}$$

with $\eta = 0.7$ approximates the numerical values much better in the interval of interest (see black line in Fig. 7). Additional terms can be included in the approximation to extend the range of validity to $P_B = 10$:

$$\Theta_{\text{MP}} \approx \eta\big(-0.001997P_B^3 + 0.006503P_B^2 + P_B + 1\big). \tag{17}$$

By using the equivalence between (14) and (15) as well as the definition of $\tilde{\theta}_B$ in (10) we obtain the value of the power of the homogeneous forward field for the SF state in the backward field:

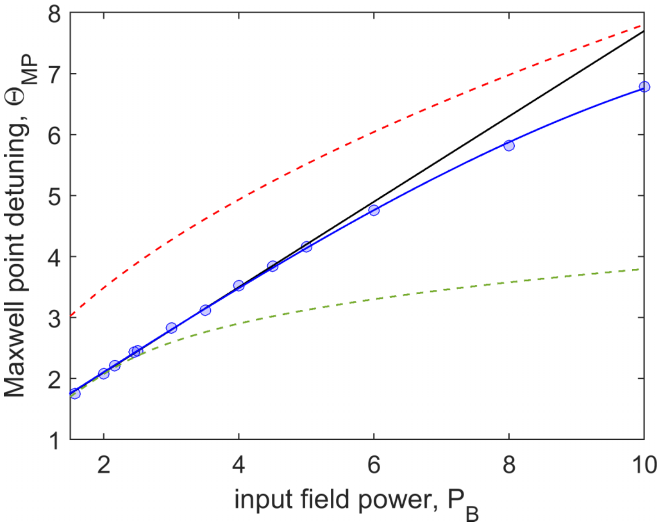

FIG. 7. The detuning Θ_{MP} of a single LLE (15) at the Maxwell point as a function of $P_B = E_B^2$. The circles are numerically evaluated points from which we obtain the linear [Eq. (16) in black] and cubic [Eq. (17) in blue] fitted curves for the Maxwell point distribution. The dashed green and dashed red curves correspond to the asymptotic and variational methods of [15], respectively.

$$\langle |F|^2 \rangle = |F|^2 = \frac{1}{\nu}[\theta_B - \Theta_{\text{MP}}] \approx \frac{1}{\nu}[\theta_B - \eta(1 + P_B)]. \tag{18}$$

As shown in the numerical simulations of the two SFs for $\theta_F < \theta_B = 3.2$ in Fig. 4(a), $|F|^2$ is independent of the control parameter θ_F and its value is just below 0.5 for the case of $P_B = 2.1609$, in agreement with (18). The power $Y_B = |B|^2$ of the homogeneous states of (15) satisfies

$$Y_B^3 - 2\Theta_{\text{MP}}Y_B^2 + \big(1 + \Theta_{\text{MP}}^2\big)Y_B - P_B = 0 \tag{19}$$

from which it is possible to obtain the values of the plateau powers Y_B^+ and Y_B^- where the SFs start and end. Note that since Θ_{MP} does not depend on θ_F, Y_B^+ and Y_B^- also do not depend on θ_F as shown in Fig. 4 for the SF states. Comparison of Y_B^+ and Y_B^- obtained from (19) with the numerical evaluation of Θ_{MP} and with the approximate expression (17) are shown in Fig. 8 in the interval of interest for P_B between 2 and 10.

It is now possible to obtain an expression for the stationary distance Δ of the two SFs. In the zero dispersion case $\beta = 0$, the SFs are vertical lines between Y_B^+ and Y_B^- so that

$$\begin{aligned} \langle |B|^2 \rangle &= \Delta Y_B^- + (1 - \Delta)Y_B^+ \\ \Delta &= \frac{Y_B^+ - \langle |B|^2 \rangle}{Y_B^+ - Y_B^-}. \end{aligned} \tag{20}$$

However, from (13) one obtains

$$\langle |B|^2 \rangle = \frac{1}{\nu}\left(\theta_F - |F|^2 \pm \sqrt{\frac{P_F}{|F|^2} - 1}\right), \tag{21}$$

where P_F is the forward input power E_F^2 and $|F|^2$ is given by Eq. (18). Hence the combinations of Eq. (19) and Eq. (21) provide an expression of the distance Δ between the two SFs

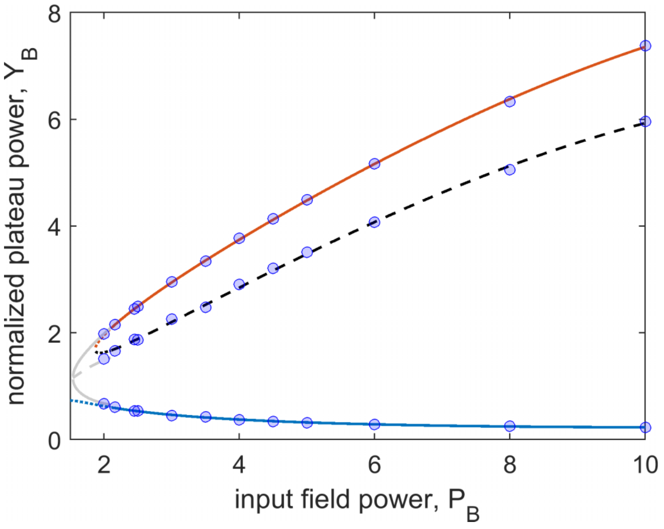

FIG. 8. Power Y_B of the homogeneous solutions before and after a SF for a single LLE at Maxwell point (19). SFs are possible after the onset of bistability at critical pump power $P_B \approx 8\sqrt{3}/9$ where the higher Y_B^+ (red) and the lower Y_B^- (blue) branches are stable but the dashed middle solution is unstable. The Maxwell point detunings Θ_{MP} are approximated by (17) for $P > 2.1$ and by an asymptotic approach for $P < 2.1$. The blue circles are homogeneous solutions before and after a SF from the simulation of (1)–(2).

at zero dispersion via Eq. (20) in terms of parameters θ_F, θ_B, P_F, P_B (see the black line in Fig. 9 for $P_F = P_B = 2.1609$, $\theta_F = 1.4$, $\theta_B = 3.2$). For dispersion different from zero, the distance Δ remains unchanged as shown in Fig. 9 for $\beta = 5$ (blue line), $\beta = 1$ (red line), $\beta = 0.1$ (green line). This means the second-order dispersion β affects the steepness of SFs but does not change the pulse duration (SF distance) of the output for noninteracting SFs.

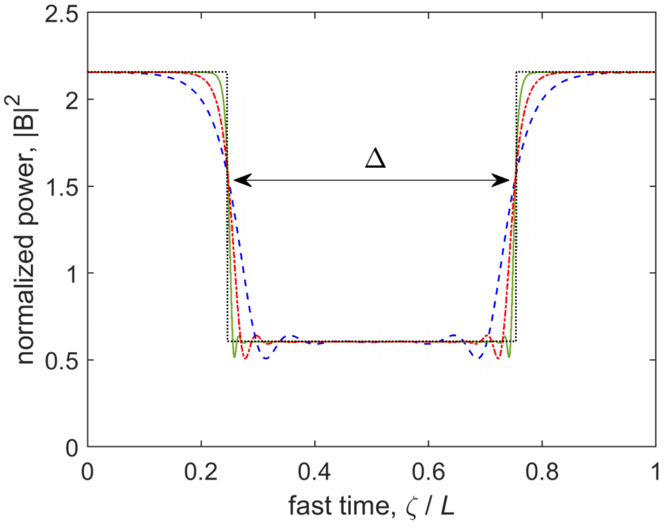

FIG. 9. Power distribution of an inhomogeneous B field exhibiting two noninteracting SFs with separation Δ for parameter values $P_F = P_B = 2.1609$, $\theta_F = 1.4$, $\theta_B = 3.2$ and dispersion coefficient $\beta = 5$ (blue dashed line), $\beta = 1$ (red dashed dotted line), $\beta = 0.1$ (green line), and $\beta = 0$ (black dotted line). Here the fast time (x axis) is normalized to the round trip time.

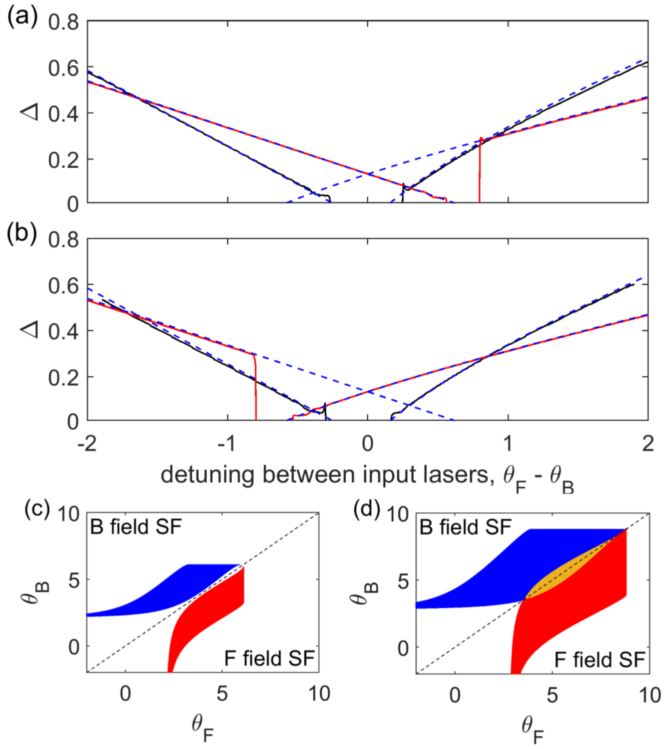

FIG. 10. (a, b) SF separation Δ when changing the detuning θ_F for fixed pump powers $P_F = P_B$ and detuning θ_B. Solid black (solid red) lines correspond to simulation results from (1)–(2) with $\beta = 1$ and for $P_F = P_B = 2.1609$, $\theta_B = 3.2$ ($P_F = P_B = 3$, $\theta_B = 5$). Panel (a) is a forward scan and (b) is a backwards scan. The blue dashed lines are the analytical results of Eqs. (20) and (26). (c, d) Range of detuning values where SF solutions exist and are stable for the B field (blue region) and for the F field (red region) or both fields (orange region), (c) $P_F = P_B = 2$ and (d) $P_F = P_B = 3$.

When using θ_F as a control parameter, expression (20) works very well when compared with the distance of two stationary SFs obtained from the simulations of (1) and (2) done with $\beta = 1$; see the left-hand side of Figs. 10(a) and 10(b). In particular we note that Δ is a function of θ_F only through $\langle |B|^2 \rangle$ as expressed in Eq. (21). This means that the distance Δ decreases linearly with θ_F with a slope given by $[\nu(Y_B^+ - Y_B^-)]^2$. Once the detuning $\theta_F < \theta_B$ and the input powers P_B and P_F are chosen, it is possible to obtain accurately the distance of the two SFs from Eq. (20) even in the regime of small distances and locked SFs (dark solitons) as shown in Fig. 10.

The conditions of validity of Eqs. (18) and (21) predict that two stable SFs can be found in the interval $\eta(1 + P_B) < \theta_B < \nu P_F + \eta(1 + P_B)$, given that $0 < \Delta < 1$. This allows us to determine regions in parameter space where vertical SF form as shown in Figs. 10(c) and 10(d). It is interesting to see that for values of $P_B > 2.145$ where stable SFs in the backward field are observed even for $\theta_F > \theta_B$, the predictions of Eq. (20) remain in good agreement with the numerical results [see red lines on the left of Figs. 10 (a) and 10(b) for $P_B = P_F = 3$].

Equations (18) and (20) suggest that precise control over the pulse duration (SF distance) of the output field is possible by simply changing the laser detuning. This allows for control over the frequency comb generation efficiency by laser parameters in contrast with conventional microresonator dark solitons, where the pulse duration is determined by the dispersion.

We now move to the case $\theta_F > \theta_B$. In this case it is the backward field B that is homogeneous and the two stable SFs are found in the forward field F. In this case the role of Eqs. (13) and (14) is exchanged:

$$E_F = (1 + i\tilde{\theta}_F)F - i|F|^2F + i\beta\partial_\zeta^2 F, \tag{22}$$

$$E_B = (1 + i\tilde{\theta}_B)B - i|B|^2B, \tag{23}$$

and one obtains $\Theta'_{\mathrm{MP}} \approx \eta(1 + P_F)$ as well as

$$\langle|B|^2\rangle = |B|^2 = \frac{1}{\nu}(\theta_F - \Theta'_{\mathrm{MP}}) \approx \frac{1}{\nu}[\theta_F - \eta(1 + P_F)]. \tag{24}$$

In the case of $\theta_F > \theta_B$, the homogeneous power of the backward field grows linearly with θ_F, which agrees with the simulation in Fig. 4(b). The form of the equation for the power $Y_F = |F|^2$, however, remains basically unchanged from Eq. (19),

$$Y_F^3 - 2\Theta'_{\mathrm{MP}}Y_F^2 + (1 + (\Theta'_{\mathrm{MP}})^2)Y_F - P_F = 0, \tag{25}$$

so that the homogeneous powers Y_F^+ and Y_F^- before and after the SFs are still independent from θ_F and, in the case of $P_F = P_B$, they have the same values of Y_B^+ and Y_B^- found for $\theta_F < \theta_B$ since $\Theta'_{\mathrm{MP}} = \Theta_{\mathrm{MP}}$. Finally,

$$\begin{aligned}\langle|F|^2\rangle &= \Delta Y_F^- + (1 - \Delta)Y_F^+ \\ \Delta &= \frac{Y_F^+ - \langle|F|^2\rangle}{Y_F^+ - Y_F^-}\end{aligned} \tag{26}$$

and

$$\langle|F|^2\rangle = \frac{1}{\nu}\left(\theta_B - |B|^2 \pm \sqrt{\frac{P_B}{|B|^2} - 1}\right). \tag{27}$$

The distance Δ depends on θ_F through $\langle|F|^2\rangle$ and then through $|B|^2$ given in Eqs. (24) and (27). At difference from the case $\theta_F < \theta_B$ this dependence is nonlinear, the slope of the curve is reversed and the distance Δ now grows with the detuning θ_F. The agreement of Eq. (26) with the numerical simulations as shown in the right hand part of Fig. 10 is again excellent. Similar to the B field case, the conditions of existence of vertical SFs for the F field is $\eta(1 + P_F) < \theta_F < \nu P_F + \eta(1 + P_F)$ given that $0 < \Delta < 1$ [see Figs. 10(c) and 10(d)].

The linear stability of SF solutions can be determined at zero dispersion using the expressions for the average field powers derived earlier in this section. Considering a SF solution in the backward field with a homogeneous forward field, their average powers are given by Eqs. (21) and (25), respectively. As calculated in Appendix B the stability of the homogeneous states before and after the SFs to spatial (fast time) perturbation are given by the eigenvalues

$$\lambda_B^+ = -1 \pm \sqrt{(\Theta_{\mathrm{MP}} - Y_B^+)(3Y_B^+ - \Theta_{\mathrm{MP}})}, \tag{28}$$

$$\lambda_B^- = -1 \pm \sqrt{(\Theta_{\mathrm{MP}} - Y_B^-)(3Y_B^- - \Theta_{\mathrm{MP}})}. \tag{29}$$

These eigenvalues depend on the pump power only. When changing the detuning θ_F, the corresponding SF solution maps into one of the multistable two-SF solutions of an LLE at Maxwell point. The homogeneous forward field eigenvalues are

$$\lambda_F = -1 \pm \sqrt{(\tilde{\theta}_F - Y_F)(3Y_F - \tilde{\theta}_F)}. \tag{30}$$

where $\tilde{\theta}_F = \theta_F - \nu\langle|B_s|^2\rangle$ is the effective detuning, and depend on θ_B implicitly through the integrated power $\langle|B|^2\rangle$.

By using the stability eigenvalues $\lambda_B^\pm$ and λ_F it is possible to determine instabilities of the SF solutions when the real part of one of these eigenvalues goes from negative to positive. For example, plateau solutions separated by SF are susceptible to Hopf bifurcations and oscillations of the homogeneous states that are connected to the SFs. This instability is introduced by perturbations to the SF states that change the average power of the field as seen in Appendix B. For the parameter values used in this work $P_F = P_B = 2.1609$, $\theta_B = 3.2$, these oscillations grow in the region $5.35 < \theta_F < 6.25$ resulting in the collapse of local structures to the HSS. Numerical simulations of Eqs. (1) and (2) confirming this instability are presented in Sec. VI.

V. EVOLUTION TOWARDS THE TWO SWITCHING-FRONT SOLUTIONS

Despite the one to one correspondence of the SF solutions of the counterpropagating system and those of the LLE at Maxwell point, the dynamics of front solutions in the counterpropagating system are different from those seen in the LLE. Here we describe the transient evolutions of a two-SF solution in the counterpropagating system as the SFs move towards the unique stationary separation of the fronts.

In Fig. 3 in Sec. III, we have seen that when the HSS of the counterpropagating system are unstable to inhomogeneous perturbations, the system relaxes to a SF solution. We consider here initial conditions made of two SFs between two homogeneous states in one field while the other field is homogeneous across the resonator. The values of the homogeneous states at the beginning and at the end of each front in the counterpropagating system depend on the average power of the fields. This means that when the SFs are not at the stationary separation, the homogeneous states are different from those of the two-SF stationary state. The values of the homogeneous power before and after a front for arbitrary separations can be calculated by considering states of the zero dispersion case of Eqs. (1) and (2), where the second-order derivative with respect to the fast time and the first-order derivative with respect to the slow time are neglected. For a two-SF solution in the B field, the upper and lower homogeneous solutions separating the SFs can be determined by solving the coupled equations

$$P_B = Y_B^3 - (\theta_B - \nu Y_F)Y_B^2 + [(\theta_F - \nu Y_F)^2 + 1]Y_B, \tag{31}$$

$$\begin{aligned}P_F = Y_F^3 &- \{\theta_F - \nu[\Delta Y_B^- + (1 - \Delta)Y_B^+]\}Y_F^2 \\ &+ (\{\theta_F - \nu[\Delta Y_B^- + (1 - \Delta)Y_B^+]\}^2 + 1)Y_F,\end{aligned} \tag{32}$$

where Y_B^+, Y_B^- are the upper and lower homogeneous solutions of the zero dispersion SF solution present in the B

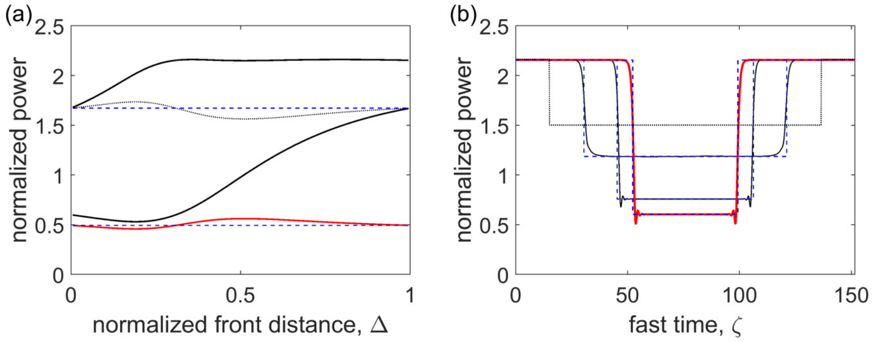

FIG. 11. (a) Power of the homogeneous states $Y_B^{\pm}$ connected by the SFs (solid black line), homogeneous field power H_F (solid red line), and average power of the field displaying SFs (dotted black line) versus the front separation is changed. The HSS in the absence of SFs is given by the dashed blue lines. (b, c) Comparison between the zero dispersion two front solutions using Eqs. (31) and (32) (dashed blue lines) and evolving two front solutions from the numerical integration of Eqs. (13) and (14) with $\beta = 0.1$ (solid lines) for shrinking front distance (b) and expanding front distance (c). The dotted black lines are the initial conditions. Parameter values are $P_F = P_B = 2.1609$, $\theta_F = 2.0$, and $\theta_B = 3.2$. The final and stationary front separation (thick red line) is $\Delta = 0.31$ in both (b) and (c).

field [solutions of Eq. (32) in a bistable state] with average power $\langle |B|^2 \rangle = \Delta Y_B^-(\Delta) + (1-\Delta)Y_B^+(\Delta)$ and Δ is the front separation. Note that the expressions for the average powers of front solutions are independent of dispersion. These solutions are plotted in Fig. 11(a).

Figures 11(b) and 11(c) show that two-SF profiles that use the solutions of Eqs. (31) and (32) with a given separation Δ provide excellent approximations to the numerical solutions of Eqs. (13) and (14) with $\beta = 0.1$ during the transition to the the final SF solution for both cases of shrinking and expanding front separation. The SFs are moving with opposite velocities and with a well-defined distance $\Delta(t)$. For each value of the slow time t and distance $\Delta(t)$, the dynamical solution is well approximated by two SFs between homogeneous states provided by Eqs. (32) given a separation distance Δ. Since for each value of θ_F there is only one stationary value of Δ, generic separations of the two SFs separated by homogeneous power from Eqs. (32) evolve in time but maintain their shape with a changing separation leading to different homogeneous powers. As such the front separation determines the power of homogeneous solutions, which in turn determines the velocity of the SFs, which in turn changes the front separation. This leads to a front velocity that depends on the front separation.

Although the shape of the transient solutions are well approximated by two vertical SFs at every moment in time, the front separation and the front velocity are nontrivial functions of time as shown in Fig. 12.

VI. OSCILLATORY DYNAMICS AND BISTABILITY WITH FRONT STATIONARY STATES

Dynamical regimes in ring resonators have been previously studied for homogeneous counterpropagating fields with symmetrical input fields and detunings [25,26]. It was seen that under the correct conditions, a pair of oppositely directed Hopf bifurcations can occur when changing the detuning $\theta_F = \theta_B$, allowing for sustained homogeneous oscillations that could exhibit period doubling bifurcations, chaos, and crisis events. In Sec. III we saw oppositely directed Hopf bifurcation for the HSS occurring when changing θ_F in an asymmetric regime of different detunings between the two counterpropagating waves since θ_B is kept fixed (see the vertical black dashed lines in Fig. 2 evidencing the interval $4.02 < \theta_F < 6.33$). These Hopf bifurcations affect the highest power HSS resulting in oscillations which are bistable with the lowest power HSS. An example of large homogeneous oscillations in the power of the two fields is displayed in Fig. 13(a) from simulations of Eqs. (1) and (2).

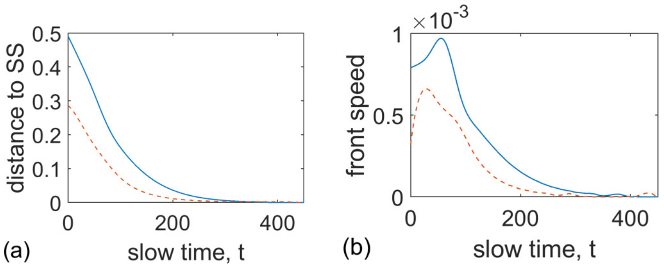

FIG. 12. Front separation (a) and front velocity (b) vs slow time while approaching a SF solution. From the data from Fig. 3, we track the front separation relative to the separation of the final SF solution in (a) and use the dimensionless slope of (a) to determine the front speed in (b). Solid blue line represents the wide initial condition, red dashed line the narrow initial condition.

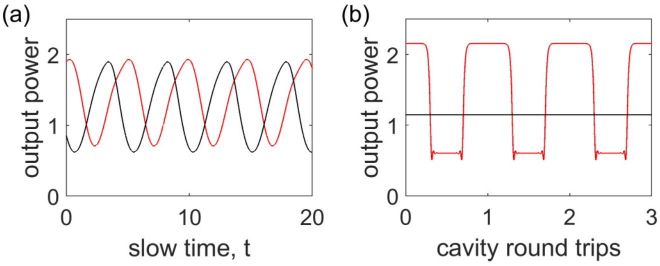

FIG. 13. Bistability of slow and fast oscillations for parameter values $\beta = 1$, $P_F = P_B = 2.1609$, $\theta_F = 4.5$, and $\theta_B = 3.2$. (a) Periodic oscillations of the homogeneous powers of both counterpropagating fields over the slow time. (b) Output power of a SF solution in the forward field (red line) and homogeneous steady state for the backward field (black line) over three cavity round trip times.

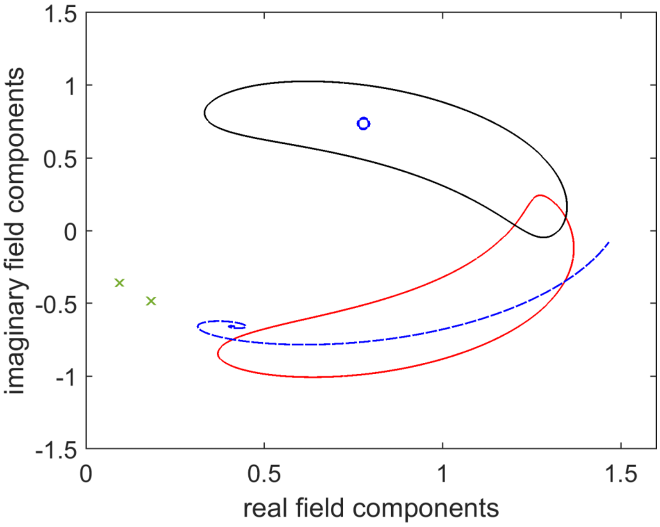

FIG. 14. Possible asymptotic states for $\beta = 1$, $P_F = P_B = 2.1609$, $\theta_F = 4.5$, and $\theta_B = 3.2$ in the phase (Argand) plane. Stable limit cycle trajectories of the homogeneous forward (red solid line) and backward (black solid line) fields; stable SF solution of the forward field (blue dashed line) and its homogeneous backward field (blue circle); stable HSS of low powers (green Xs for forward and backward fields).

In the parameter region of Fig. 13, the HSS of large powers are unstable not only to homogeneous oscillations but also to local perturbations on the fast timescale (see the line marked with X in the interval $3.35 < \theta_F < 6.47$ in Fig. 2). We find that depending on the initial condition, the system can evolve to either the homogeneous oscillations of Fig. 13(a) or to a SF solution in the forward field with a homogeneous backward field [see Fig. 13(b)] or to a HSS corresponding to low powers. To display the richness of possible asymptotic states of Eqs. (1) and (2), we show in Fig. 14 the asymptotic trajectories of oscillating homogeneous fields, the asymptotic trajectories of the SF state and the asymptotic points of the HSS of low powers in the phase (Argand) plane for the same parameters of Fig. 13. Depending on the initial condition, the microring device can evolve to any of these three final states generating either large-amplitude slow oscillations in both fields, or large-amplitude fast oscillations in just one field (the forward one) or no output oscillations at all. This provides the operator with a remarkable number of output waveforms with possible selection of each one by suitable perturbation of the input fields (in their amplitude or phase). It is possible to generate light plateau states using a transient pulsing input field containing sudden step to provide perturbations to the HSS.

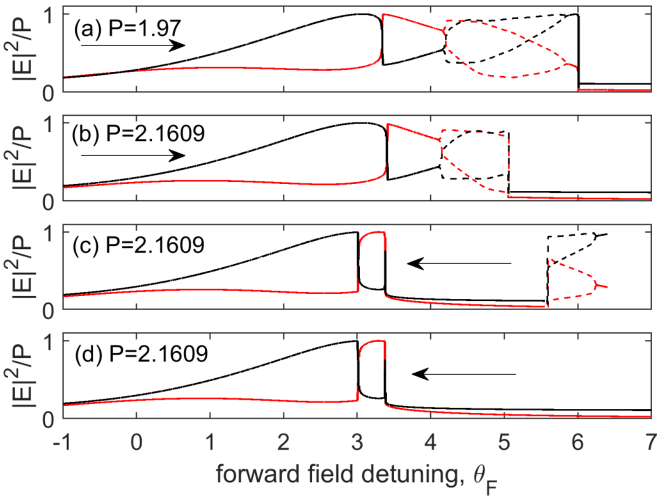

FIG. 15. Homogeneous field powers (black line backward field, red line forward field) when scanning the detuning θ_F for fixed detuning $\theta_B = 3.2$ and fixed equal pump powers $P = P_F = P_B$. Dashed lines correspond to the power extrema during oscillation. (a) Forward scan for $P = 1.95$. Limit cycle oscillations are present in the detuning range $4.2 < \theta_F < 5.9$. (b) Forward scan for $P = 2.1609$. Limit cycle oscillations are present in the detuning range $4.1 < \theta_F < 5.1$. (c) Backward scan for $P = 2.1609$ starting at $\theta_F = 6.4$. Limit cycle oscillations are present in the detuning range $5.5 < \theta_F < 6.2$. (d) Backward scan for $P = 2.1609$ starting at $\theta_F = 7.0$. No oscillations observed.

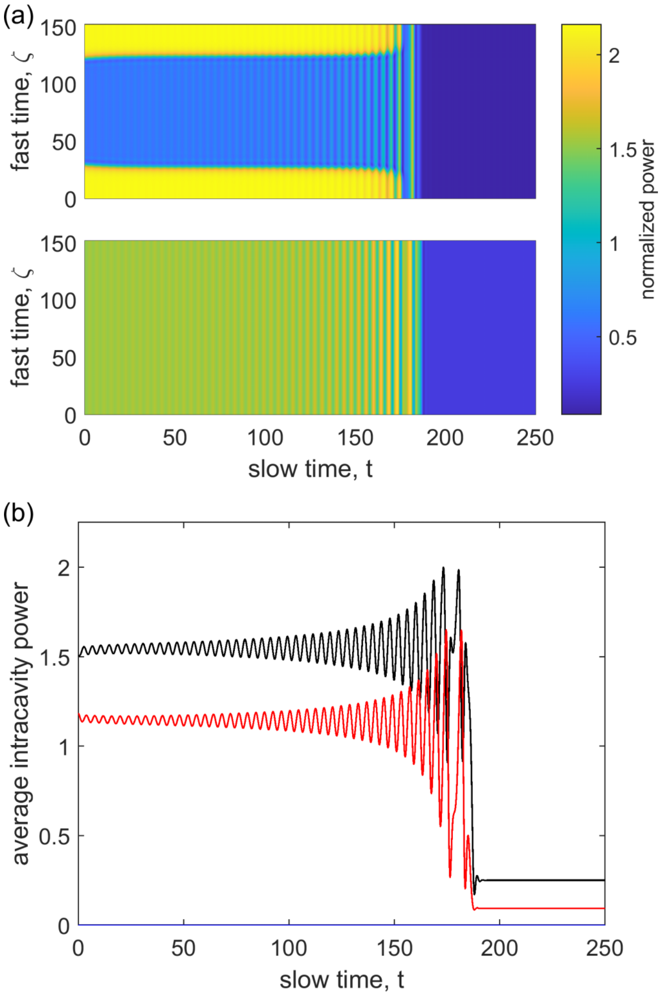

FIG. 16. Dynamical evolution from an initial condition of a two-SF solution in the forward field and a homogeneous solution in the backward field for $P_F = P_B = 2.1609$, $\theta_F = 5.3$, $\theta_B = 3.2$. Oscillations grow until both fields reach the stable HSS of low powers. (a) Intracavity power of the forward (upper) and backward (lower) fields over slow time. (b) Average interactivity power of the forward (red) and backward (black) over slow time.

When scanning the forward detuning for the parameter values studied here, we do not observe period doubling bifurcations or deterministic chaos at difference with typical simulations at parameter symmetry [25–27]. We observe, however, sudden crises when the stable trajectory of the limit cycle can intersect the unstable HSS in the regions of multiple stationary states. This results in sudden instabilities of the oscillations, which collapse to the lower stable HSS. In Fig. 15 we show simulations of counterpropagating fields when scanning the detuning θ_F forwards and backwards. Forward and backward Hopf bifurcations can be clearly seen in the forward scan at $P_F = P_B = 1.95$ in Fig. 15(a) where the dotted lines represent the maxima and minima of the oscillating powers of the homogeneous fields over slow time variations. When increasing the input power, attractor crises are observed both in the forward (at $\theta_F \approx 5.05$) and in the backward (at $\theta_F \approx 5.62$) scans [see Figs. 15(b) and 15(c)] leading to a transfer to the low-power HSS. Note, however, that depending on the initial condition of the backward scan, there is the possibility of observing no oscillations and no crises as displayed in Fig. 15(d).

Figure 15 focuses on homogeneous oscillations and HSS of low powers. The situation is further complicated by the presence of SF states in the forward field with a homogeneous backward field. When changing θ_F there is a further temporal instability of the SF solutions which causes the homogeneous states connecting the SFs to start to oscillate resulting in the entire inhomogeneous structure to oscillate, along with homogeneous oscillations of the backward field. For $\theta_F < 5.35$ these oscillations are damped allowing for stable SF states, but for $5.35 < \theta_F < 6.25$ such oscillations grow, destroying fast time structures and the system moves to the HSS corresponding to low powers as shown in Fig. 16.

VII. CONCLUSIONS

We have investigated the effects of global average coupling induced by the interaction of two input beams counterpropagating in a ring resonator with normal dispersion. In particular, we find stationary states of light plateaus that are separated by two switching fronts. By controlling the input laser frequency detuning, the propagation direction of the light plateau states can be switched between clockwise and counterclockwise. We have derived semianalytical expressions of the distance between stable switching fronts and the powers of the plateaus as a function of the detunings. These expressions rely on the knowledge of the Maxwell point location in the parameter space of the LLE. By using a numerical fit from LLE simulations, we found excellent agreement between the obtained formulas and the numerical simulations. Maxwell point locations can also be determined by asymptotic or variational approaches [15] but at the detriment of the agreement with numerical simulations. Apart from being present in only one of the two conterpropagating fields, light plateaus in our global system are unusual in that they have power values different from the homogeneous steady states of the system. Global average coupling introduces a balancing of areas associated with the two plateau powers resulting in a controllable distance of two stationary SFs by the detunings, which in turn can be tuned by changing the frequency of the input fields. Robust SF solutions are present for large ranges of detuning allowing great control over the distance of the two SFs through the laser parameters. This allows the user to precisely control the pulse duration of the output field, and hence the frequency comb generation efficiency by changing the input fields detuning. The second-order dispersion determines the steepness of SFs with no effect on the pulse duration when well separated. This is different from conventional microresonator dark and bright solitons, whose width is determined by second-order dispersion. In addition we find that changing the laser detuning across the symmetric state results in the SF solutions to disappear from one field and then to reappear in the other field. This results in the SFs switching direction in the microresonator while scanning a single detuning parameter thus allowing for a corresponding switch of the beam where a frequency comb is generated.

The analytic description of SF and plateaus extends to transient states, allowing us to describe the changes of plateau power and SFs separation as they move towards the final stationary state corresponding to a given SF separation.

We have also investigated oscillations in symmetry broken ($\theta_F \neq \theta_B$) counterpropagation. We have identified stable limit cycle oscillations in detuning symmetry-broken regimes, and observed sudden crisis in which the oscillations become unstable due to a collision with an unstable HSS. Stable oscillatory dynamics coexist with SF solutions for large ranges of parameter values. We have even identified a multistability of oscillations with SF solutions and the lowest power homogeneous stationary state. Depending on the initial condition, the microring device can evolve to any of these three final states generating either large-amplitude slow oscillations in both fields, or large-amplitude fast oscillations in just one field or no output oscillations at all. This provides the operator with a remarkable number of output waveforms with possible selection of each one by suitable perturbation of the input fields (in their amplitude or phase).

Microresonator systems have undergone much study in recent years. All our predictions have been obtained for realistic parameters with possible experimental verification in a variety of ring resonator setups, from microring to fiber loops. Frequency comb generation has also been demonstrated using two lasers for bichromatic pumping of a microring resonator for the generation of dark bright solitons [33]. A modification to this setup to incorporate bidirectional pumping should allow for the generation of counterpropagating SF states. Single-input laser setups in the presence of backscattering have indeed predicted and observed Maxwell point front solutions in microring resonators [14,15]. Backscattering of the pump laser results in a counterpropagating field, allowing for a single-laser setup to produce plateaus that can be the result of extending our model to these configurations.

Configurations of alternating SF and light plateaus in only one field are not just interesting for their fundamental features being related to global coupling of two waves and integro-partial-differential equations. The robust, highly configurable, and controllable SFs solutions of counterpropagating light can be useful in many real world applications such as all optical oscillators, optical computing, time reversal symmetry breaking, and signal routing in telecommunication systems. Future considerations for this system include a pulse driving configuration in one or both of the input fields. The results of this paper can be further enhanced by polarization considerations of the counterpropagating fields. This would introduce additional spontaneous symmetry breaking between polarization modes similar to those observed in [34–36].

ACKNOWLEDGMENTS

This research was supported by funding from the EPSRC DTA Grant No. EP/T517938/1. P.D. acknowledges support by the H2020 European Research Council (ERC) (756966, Counterlight), the Marie Sklodowska-Curie Innovative Training Network (MSCA) (812818, Microcombs), and the Max Planck Society.

APPENDIX A: LINEAR STABILITY OF HOMOGENEOUS STATIONARY STATES TO INHOMOGENEOUS PERTURBATION IN COUNTERPROPAGATION

Here we investigate the stability of stationary homogeneous states F_s, B_s to spatial perturbations at zero dispersion ($\beta = 0$). The nonlocality of the counterpropagating system means that local perturbations will result in changes to the unperturbed regions and therefore have an implicit dependence on the entirety of the field. It is necessary to track the evolution of the entire field to determine the susceptibility of the homogeneous stationary states to spatial bifurcation. We do so by considering the field partwise in fast time

$$F = F_1 T(\zeta) T(x_F - \zeta) + F_2 T(\zeta - x_F) T(L - \zeta), \tag{A1}$$

$$B = B_1 T(\zeta) T(x_B - \zeta) + B_2 T(\zeta - x_B) T(L - \zeta), \tag{A2}$$

such that

$$|F|^2 = |F_1|^2 T(\zeta) T(x_F - \zeta) + |F_2|^2 T(\zeta - x_F) T(L - \zeta), \tag{A3}$$

$$|B|^2 = |B_1|^2 T(\zeta) T(x_B - \zeta) + |B_2|^2 T(\zeta - x_B) T(L - \zeta), \tag{A4}$$

where $T(\zeta)$ represents the Heaviside step function which has the value 1 for $\zeta \geqslant 0$ and 0 for $\zeta < 0$, and x_F, x_B are the lengths of fast time occupied by F_1, B_1. The partwise fields F_1 and F_2 (B_1 and B_2) represent two separate domains of fast time with different spatially homogeneous perturbations of the same HSS, such that the combined perturbation is spatially inhomogeneous. We consider the linear perturbation to the counterpropagating system of the form

$$F_1 = F_s + f_1, \quad F_2 = F_s + f_2, \tag{A5}$$

$$B_1 = B_s + b_1, \quad B_2 = B_s + b_2. \tag{A6}$$

The average field powers under this formulation are

$$\langle |F|^2 \rangle = \Delta_F |F_1|^2 + (1 - \Delta_F)|F_2|^2, \tag{A7}$$

$$\langle |B|^2 \rangle = \Delta_B |B_1|^2 + (1 - \Delta_B)|B_2|^2, \tag{A8}$$

where $\Delta_F = x_F/L$, $\Delta_B = x_B/L$, are the normalized lengths occupied by F_1, B_1. The evolution of the F_1 and F_2 components are not explicitly dependent on each other due to zero dispersion. As such we describe the evolution of the F field as separate ODEs for F_1, F_2 (likewise for the B field), hence this system is described by the four ODEs

$$\partial_\tau F_1 = S_F - (1 + i\theta_F)F_1 + i\{|F_1|^2 + \nu[\Delta_B |B_1|^2 + (1 - \Delta_B)|B_2|^2]\}F_1, \tag{A9}$$

$$\partial_\tau F_2 = S_F - (1 + i\theta_F)F_2 + i\{|F_2|^2 + \nu[\Delta_B |B_1|^2 + (1 - \Delta_B)|B_2|^2]\}F_2, \tag{A10}$$

$$\partial_\tau B_1 = S_B - (1 + i\theta_B)B_1 + i\{|B_1|^2 + \nu[\Delta_F |F_1|^2 + (1 - \Delta_F)|F_2|^2]\}B_1, \tag{A11}$$

$$\partial_\tau B_2 = S_B - (1 + i\theta_B)B_2 + i\{|B_2|^2 + \nu[\Delta_F |F_1|^2 + (1 - \Delta_F)|F_2|^2]\}B_2. \tag{A12}$$

Without loss of generality, we adjust the phase of F, B such that F_s, B_s are real. We have that the real and imaginary components of the perturbation evolve as

$$\frac{d}{d\tau}\begin{pmatrix} f_{1,\mathrm{r}} \\ f_{1,\mathrm{i}} \\ f_{2,\mathrm{r}} \\ f_{2,\mathrm{i}} \\ b_{1,\mathrm{r}} \\ b_{1,\mathrm{i}} \\ b_{2,\mathrm{r}} \\ b_{2,\mathrm{i}} \end{pmatrix} = \begin{pmatrix} -1 & A_1 & 0 & 0 & 0 & 0 & 0 & 0 \\ -B_1 & -1 & 0 & 0 & -\Delta_B C & 0 & -(1-\Delta_B)C & 0 \\ 0 & 0 & -1 & A_1 & 0 & 0 & 0 & 0 \\ 0 & 0 & -B_1 & -1 & -\Delta_B C & 0 & -(1-\Delta_B)C & 0 \\ 0 & 0 & 0 & 0 & -1 & A_2 & 0 & 0 \\ -\Delta_F C & 0 & -(1-\Delta_F)C & 0 & -B_2 & -1 & 0 & 0 \\ 0 & 0 & 0 & 0 & 0 & 0 & -1 & A_2 \\ -\Delta_F C & 0 & -(1-\Delta_F)C & 0 & 0 & 0 & -B_2 & -1 \end{pmatrix}\begin{pmatrix} f_{1,\mathrm{r}} \\ f_{1,\mathrm{i}} \\ f_{2,\mathrm{r}} \\ f_{2,\mathrm{i}} \\ b_{1,\mathrm{r}} \\ b_{1,\mathrm{i}} \\ b_{2,\mathrm{r}} \\ b_{2,\mathrm{i}} \end{pmatrix}, \tag{A13}$$

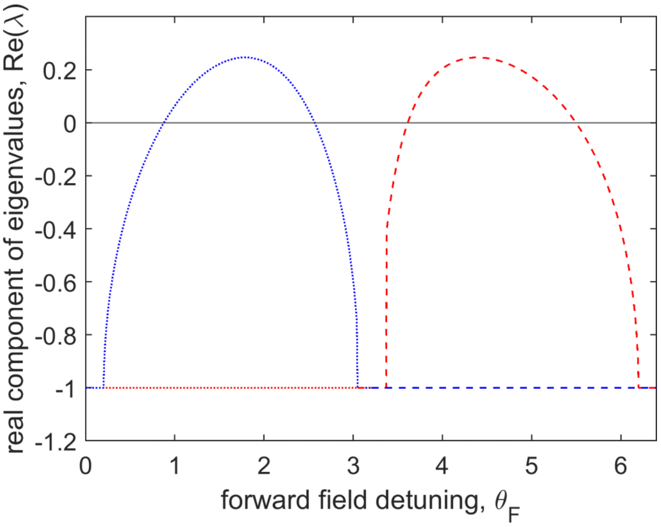

FIG. 17. Real component of eigenvalues for changing θ_F with parameter values $P_F = P_B = 2.1609, \theta_B = 3.2$. The corresponding HSS are plotted in Fig. 2. For $\theta_F > \theta_B$ (dashed lines) we consider the highest power branch of HSS. For $\theta_F < \theta_B$ (dotted lines) we consider the sole HSS. The real components of the "+" solutions of Eqs. (A16) and (A17) indicate instability. Plotted above are the "+" solutions of λ_F (red) and λ_B (blue).

where $A_1 = F_s^2 + \nu B_s^2 - \theta_F$, $A_2 = B_s^2 + \nu F_s^2 - \theta_B$, $B_1 = 3F_s^2 + \nu B_s^2 - \theta_F$, $B_2 = 3B_s^2 + \nu F_s^2 - \theta_B$, and $C = 2\nu F_s B_s$. This results in the known eigenvalues of homogeneous perturbation of the homogeneous stationary states [25]

$$\lambda = -1 \pm \frac{\sqrt{-A_1B_1 - A_2B_2 \pm S}}{\sqrt{2}}, \tag{A14}$$

$$S = \sqrt{(A_1B_1 - A_2B_2)^2 + 4A_1A_2C^2} \tag{A15}$$

with additional eigenvalues indicative of instability of either the F field (λ_F) or the B field (λ_B) due to spatially inhomogeneous perturbations

$$\lambda_F = -1 \pm \sqrt{-A_1B_1}, \tag{A16}$$

$$\lambda_B = -1 \pm \sqrt{-A_2B_2}. \tag{A17}$$

These four eigenvalues are a consequence of the global coupling and are not present in local coupling regime of copropagating fields. Figure 17 shows the real component of the of '+' eigenvalues [Eqs. (A16) and (A17)] of the HSS shown in Fig. 2. The HSS is unstable when the real component is positive and are marked with the symbol X in Fig. 2. They are identical to those seen in two single LLEs with parameter values $P_F, \tilde{\theta}_F$ & $P_B, \tilde{\theta}_B$. We note that F_1, F_2 do not need to be continuous regions of fast time. They represent the total proportion of the field perturbed below or above the stationary solution and as such the above eigenvalues are appropriate for a random spatial perturbation (which would have width $\Delta_F \approx 0.5$), and likewise for the B field.

In the regime of local coupling, the two copropagating fields are coupled by Kerr cross-phase modulation. As such a local spatial perturbation of one of the fields will only effect the corresponding spatial region of the other field. If we introduce a step function perturbation to the homogeneous stationary states F_s, B_s with size Δ of the form $F = F_s + fT(\zeta)T(\Delta - \zeta/L)$, $B = B_s + bT(\zeta)T(\Delta - \zeta/L)$, the perturbations f, b will evolve identically to a homogeneous perturbation of the entire field. This results in the eigenvalues given by Eq. (A14) of homogeneous perturbation of the homogeneous stationary states [25]. Nonlocality in the counterpropagating system introduces an implicit dependence on the power of the entire field. This allows the system to access inhomogeneous states of the single LLE and introduces four additional eigenvalues indicative of spatial instability.

APPENDIX B: LINEAR STABILITY OF INHOMOGENEOUS FRONT STATIONARY STATES IN COUNTERPROPAGATING FIELDS

In numerical simulations, we observe that stationary SFs form in only one field at any a given time, with the other field remaining homogeneous. Using a similar framework as in Appendix A, we can simply do the analysis by considering a homogeneous F field with an inhomogeneous B field. We describe the B field as the partwise function in terms of the higher and lower power homogeneous state B^+, B^- connected by the SFs, and the F field as a single homogeneous function. At zero dispersion we have

$$B = B^-T(\zeta)T(\Delta_B - \zeta/L) + B^+T(\zeta/L - \Delta_B)T(1 - \zeta/L), \tag{B1}$$

where Δ is the normalized front separation. Therefore

$$|F|^2 = |F|^2, \tag{B2}$$

$$|B|^2 = |B^-|^2T(\zeta)T(\Delta_B - \zeta/L) + |B^+|^2T(\zeta/L - \Delta_B)T(1 - \zeta/L), \tag{B3}$$

and the average field power is

$$\langle |F|^2 \rangle = |F|^2, \tag{B4}$$

$$\langle |B|^2 \rangle = \Delta_B|B^-|^2 + (1 - \Delta_B)|B^+|^2. \tag{B5}$$

As the B field is partwise and the F field is homogeneous, the evolution of the F, B fields is described by the three ODEs

$$\partial_\tau F = S_F - (1 + i\theta_F)F + i\{|F|^2 + \nu[\Delta_B|B^-|^2 + (1 - \Delta_B)|B^+|^2]\}F, \tag{B6}$$

$$\partial_\tau B^+ = S_B - (1 + i\theta_B)B^+ + i(|B^+|^2 + \nu|F|^2)B^+, \tag{B7}$$

$$\partial_\tau B^- = S_B - (1 + i\theta_B)B^- + i(|B^-|^2 + \nu|F|^2)B^-. \tag{B8}$$

We introduce a linear perturbation to the system that is spatially inhomogeneous in the B field and homogeneous in the F field,

$$F = F_s + f, \tag{B9}$$

$$B^+ = B_s^+ + b^+, \quad B^- = B_s^- + b^-, \tag{B10}$$

where F_s is the stationary homogeneous solution of the F field and B_s^+, B_s^- are the two homogeneous stationary states connected by the SFs. Here we consider the real part of the fields $F_{\mathrm{s}}, B_{\mathrm{s}}$ such that the real and imaginary components of the perturbations evolve as

$$\frac{d}{d\tau}\begin{pmatrix} f_{\mathrm{r}} \\ f_{\mathrm{i}} \\ b_{\mathrm{r}}^{+} \\ b_{\mathrm{i}}^{+} \\ b_{\mathrm{r}}^{-} \\ b_{\mathrm{i}}^{-} \end{pmatrix} = \begin{pmatrix} -1 & A & 0 & 0 & 0 & 0 \\ -B & -1 & -(1-\Delta_B)C_1 & 0 & -\Delta_B C_2 & 0 \\ 0 & 0 & -1 & A_1 & 0 & 0 \\ -C_1 & 0 & -B_1 & -1 & 0 & 0 \\ 0 & 0 & 0 & 0 & -1 & A_2 \\ -C_2 & 0 & 0 & 0 & -B_2 & -1 \end{pmatrix}\begin{pmatrix} f_{\mathrm{r}} \\ f_{\mathrm{i}} \\ b_{\mathrm{r}}^{+} \\ b_{\mathrm{i}}^{+} \\ b_{\mathrm{r}}^{-} \\ b_{\mathrm{i}}^{-} \end{pmatrix}, \tag{B11}$$

where $A = F_{\mathrm{s}}^2 + \nu\langle|B_{\mathrm{s}}|^2\rangle - \theta_F$, $B = 3F_{\mathrm{s}}^2 + \nu\langle|B_{\mathrm{s}}|^2\rangle - \theta_F$, $A_1 = (B_{\mathrm{s}}^{+})^2 + \nu F_{\mathrm{s}}^2 - \theta_B$, $B_1 = 3(B_{\mathrm{s}}^{+})^2 + \nu F_{\mathrm{s}}^2 - \theta_B$, $A_2 = (B_{\mathrm{s}}^{-})^2 + \nu F_{\mathrm{s}}^2 - \theta_B$, $B_2 = 3(B_{\mathrm{s}}^{-})^2 + \nu F_{\mathrm{s}}^2 - \theta_B$, $C_1 = 2\nu F_{\mathrm{s}} B_{\mathrm{s}}^{+}$, $C_2 = 2\nu F_{\mathrm{s}} B_{\mathrm{s}}^{-}$. This results in the characteristic polynomial

$$\begin{aligned} 0 = {} & [(\lambda+1)^2 + A_2B_2]\{[(\lambda+1)^2 + AB][(\lambda+1)^2 + A_1B_1] - 2\Delta_B A A_1 C_1^2\} \\ & + [(\lambda+1)^2 + A_1B_1]\{[(\lambda+1)^2 + AB][(\lambda+1)^2 + A_2B_2] - 2(1-\Delta_B) A A_2 C_2^2\}, \end{aligned} \tag{B12}$$

which is composed of the product of terms indicative of spatial instability

$$\Lambda_n^{\pm} = \lambda + 1 \pm \sqrt{-A_nB_n} \tag{B13}$$

and eigenvalues indicative of temporal instability (in the curly brackets)

$$L_n^{(\pm,\pm)} = \lambda + 1 \pm \frac{\sqrt{-AB - A_nB_n \pm S_n}}{\sqrt{2}}, \qquad S_n = \sqrt{(AB - A_nB_n)^2 + (-1)^n(1 - n - \Delta_B)8AA_nC_n^2}. \tag{B14}$$

This expression has similar form the characteristic polynomial of HSS seen in Appendix A and will become identical when $\Delta_B = 0, 1$. In simulation, we observe that the SF solutions are susceptible to damped oscillations under perturbation. Figure 18 shows the real component of the eigenvalues of SF solutions for parameters $P_F = P_B = 2.1609$, $\theta_B = 3.2$. In the range $5.35 < \theta_F < 6.25$ the real components become positive such that oscillations of the upper and lower power plateaus grow until both fields reach a stable HSS.

If we instead consider a spatially inhomogeneous perturbation to the homogeneous plateau of the SF solution present in the backward field, that does not change the average power of the field $\langle|B_{\mathrm{s}} + b(\zeta)|^2\rangle = \langle|B_{\mathrm{s}}|^2\rangle$, then the resulting eigenvalues are

$$\lambda = -1 \pm \sqrt{-AB}, \qquad \text{forward field}, \tag{B15}$$

$$\lambda_n = -1 \pm \sqrt{-A_nB_n}, \qquad \text{backward field}. \tag{B16}$$

These eigenvalues are indicative of the spatial stability of the two HS connected to the SFs. This suggests that temporal instability of the stationary states of counterpropagating fields is observed when the integrated powers of the fields are perturbed. Otherwise the fields exhibit the stability of an LLE with effective detuning as defined in Sec. IV. In particular, the eigenvalues of the SF solution at stationary separation as calculated in Sec. IV are those of a single LLE at Maxwell point

$$\lambda^{+} = -1 \pm \sqrt{(\Theta_{\mathrm{MP}} - Y_B^{+})(3Y_B^{+} - \Theta_{\mathrm{MP}})}, \tag{B17}$$

$$\lambda^{-} = -1 \pm \sqrt{(\Theta_{\mathrm{MP}} - Y_B^{-})(3Y_B^{-} - \Theta_{\mathrm{MP}})}. \tag{B18}$$

This is expected due to the one to one correspondence of the counterpropagating SF solution to the stationary states of the LLE. We note that these eigenvalues are independent of the detuning values. As such the solutions map to the identical Maxwell point LLE when changing θ_F which exhibits a multistability of SF states. The eigenvalues of the forward field are

$$\lambda = -1 \pm \sqrt{(\tilde{\theta}_F - Y_F)(3Y_F - \tilde{\theta}_F)}, \tag{B19}$$

where $\tilde{\theta}_F = \theta_F - \nu\langle|B_{\mathrm{s}}|^2\rangle$ is the effective detuning which is dependent on the detuning values (or more specifically the front separation Δ).

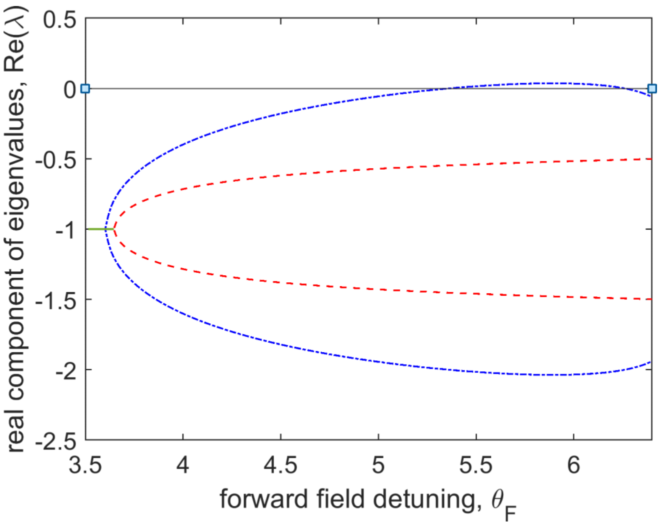

FIG. 18. Real component of eigenvalues of the zero dispersion SF solutions for changing θ_F with parameter values $P_F = P_B = 2.1609$, $\theta_B = 3.2$. The six eigenvalues are calculated numerically [six roots of Eq. (B12)], where each branch of the blue dot dashed line represents the real part of a complex conjugate pair of solutions; the red dashed lines are real solutions.

[1] A. Pasquazi, M. Peccianti, l. Razzari, D. J. Moss, S. Coen, M. Erkintalo, Y. K. Chembo, T. Hansson, S. Wabnitz, P. Del'Haye, X. Xue, A. M. Weiner, and R. Morandotti, Micro-combs: A novel generation of optical sources, Phys. Rep. **729**, 1 (2018).

[2] J. Pfeifle, V. Brasch, M. Lauermann, Y. Yu, D. Wegner, T. Herr, K. Hartinger, P. Schindler, J. Li, Da. Hillerkuss *et al.*, Coherent terabit communications with microresonator Kerr frequency combs, Nat. Photonics **8**, 375 (2014).

[3] J. Pfeifle, A. Coillet, R. Henriet, K. Saleh, P. Schindler, C. Weimann, W. Freude, I. V. Balakireva, L. Larger, C. Koos *et al.*, Optimally Coherent Kerr Combs Generated with Crystalline Whispering Gallery Mode Resonators for Ultrahigh Capacity Fiber Communications, Phys. Rev. Lett. **114**, 093902 (2015).

[4] M.-G. Suh, Q.-F. Yang, K. Y. Yang, X. Yi, and K. J. Vahala, Microresonator soliton dual-comb spectroscopy, Science **354**, 600 (2016).

[5] A. Dutt, C. Joshi, X. Ji, J. Cardenas, Y. Okawachi, K. Luke, A. L. Gaeta, and M. Lipson, On-chip dual-comb source for spectroscopy, Sci. Adv. **4**, e1701858 (2018).

[6] S. Coen and M. Erkintalo, Temporal cavity solitons in Kerr media, in *Nonlinear Optical Cavity Dynamics: From Microresonators to Fiber Lasers*, edited by P. Grelu (John Wiley & Sons, New York, 2015), pp. 11–40.

[7] L. Lugiato and R. Lefever, Spatial Dissipative Structures in Passive Optical Systems, Phys. Rev. Lett. **58**, 2209 (1987).

[8] M. Haelterman, S. Trillo, and S. Wabnitz, Dissipative modulation instability in a nonlinear dispersive ring cavity, Opt. Commun. **91**, 401 (1992).

[9] L. A. Lugiato, F. Prati, M. L. Gorodetsky, and T. J. Kippenberg, From the Lugiato–Lefever equation to microresonator-based soliton Kerr frequency combs, Phil. Trans. R. Soc. A. **376**, 20180113 (2018).

[10] N. M. Kondratiev and V. E. Lobanov, Modulational instability and frequency combs in whispering-gallery-mode microresonators with backscattering, Phys. Rev. A **101**, 013816 (2020).

[11] D. V. Skryabin, Hierarchy of coupled mode and envelope models for bi-directional microresonators with Kerr nonlinearity, OSA Continuum **3**, 1364 (2020).

[12] W. J. Firth, L. Columbo and A. J. Scroggie, Proposed Resolution of Theory-Experiment Discrepancy in Homoclinic Snaking, Phys. Rev. Lett. **99**, 104503 (2007).

[13] Z. Fan and D. V. Skryabin, Soliton blockade in bidirectional microresonators, Opt. Lett. **45**, 6446 (2020).

[14] S.-P. Yu, E. Lucas, J. Zang, and S. B. Papp, A continuum of bright and dark pulse states in a photonic-crystal resonator, Nat. Commun. **13**, 3134 (2022).

[15] H. Wang, B. Shen, L. Wu, C. Bao, W. Jin, L. Chang, M. A. Leal, A. Feshali, M. Paniccia, J. E. Bowers *et al.*, Self-regulating soliton domain walls in microresonators, arXiv:2103.10422 (2021).

[16] P. C. Fife and J. B. McLeod, The approach of solutions of nonlinear diffusion equations to travelling front solutions, Arch. Rational Mech. Anal. **65**, 335 (1977).

[17] N. N. Rosanov, *Spatial Hysteresis and Optical Patterns* (Springer, Berlin, 2002).

[18] P. Parra-Rivas, D. Gomila, E. Knobloch, S. Coen, and L. Gelens, Origin and stability of dark pulse Kerr combs in normal dispersion resonators, Opt. Lett. **41**, 2402 (2016).

[19] B. Garbin, Y. Wang, S. G. Murdoch, G.-L. Oppo, S. Coen, and M. Erkintalo, Experimental and numerical investigations of switching wave dynamics in a normally dispersive fibre ring resonator, Eur. Phys. J. D **71**, 240 (2017).

[20] P. Coullet, J. Lega, B. Houchmandzadeh, and J. Lajzerowicz, Breaking Chirality in Nonequilibrium Systems, Phys. Rev. Lett. **65**, 1352 (1990).

[21] G.-L. Oppo, A. J. Scroggie, and W. J. Firth, From domain walls to localized structures in degenerate optical parametric oscillators, J. Opt. B: Quantum Semiclass. Opt. **1**, 133 (1999).

[22] G.-L. Oppo, A. J. Scroggie, and W. J. Firth, Characterization, dynamics and stabilization of diffractive domain walls and dark ring cavity solitons in parametric oscillators, Phys. Rev. E **63**, 066209 (2001).

[23] M. Gilles, P.-Y. Bony, J. Garnier, A. Picozzi, M. Guasoni, and J. Fatome, Polarization domain walls in optical fibres as topological bits for data transmission, Nat. Photonics **11**, 102 (2017).

[24] B. Garbin, J. Fatome, G.-L. Oppo, M. Erkintalo, S. G. Murdoch, and S. Coen, Dissipative Polarization Domain Walls in a Passive Coherently Driven Kerr Resonator, Phys. Rev. Lett. **126**, 023904 (2021).

[25] M. T. M. Woodley, J. M. Silver, L. Hill, F. Copie, L. Del Bino, S. Zhang, G.-L. Oppo, and P. Del'Haye, Universal symmetry-breaking dynamics for the Kerr interaction of counterpropagating light in dielectric ring resonators, Phys. Rev. A **98**, 053863 (2018).

[26] M. T. M. Woodley, L. Hill, L. Del Bino, G.-L. Oppo, and P. Del'Haye, Self-Switching Kerr Oscillations of Counterpropagating Light in Microresonators, Phys. Rev. Lett. **126**, 043901 (2021).

[27] L. Hill, G.-L. Oppo, M. T. M. Woodley, and P. Del'Haye, Effects of self-and cross-phase modulation on the spontaneous symmetry breaking of light in ring resonators, Phys. Rev. A **101**, 013823 (2020).

[28] L. Del Bino, M. J. Silver, M. T. M. Michael, L. S. Stebbings, X. Zhao, and P. Del'Haye, Microresonator isolators and circulators based on the intrinsic nonreciprocity of the Kerr effect, Optica **5**, 279 (2018).

[29] L. Del Bino, N. Moroney, and P. Del'Haye, Optical memories and switching dynamics of counterpropagating light states in microresonators, Opt. Express **29**, 2193 (2021).

[30] P. Parra-Rivas, E. Knobloch, D. Gomila, and L. Gelens, Dark solitons in the Lugiato-Lefever equation with normal dispersion, Phys. Rev. A **93**, 063839 (2016).

[31] X. Xue, Y. Xuan, Y. Liu, P.-H. Wang, S. Chen, J. Wang, D. E. Leaird, M. Qi, and A. M. Weiner, Mode-locked dark pulse Kerr combs in normal-dispersion microresonators, Nat. Photonics **9**, 594 (2015).

[32] X. Xue, P.-H. Wang, Y. Xuan, M. Qi, and A. M. Weiner, Microresonator Kerr frequency combs with high conversion efficiency, Laser Photonics Rev. **11**, 1600276 (2017).

[33] S. Zhang, T. Bi, G. N. Ghalanos, N. P. Moroney, L. Del Bino, and P. Del'Haye, Dark-Bright Soliton Bound States in a Microresonator, Phys. Rev. Lett. **128**, 033901 (2022).

[34] B. Garbin, J. Fatome, G. L. Oppo, M. Erkintalo, G. S. Murdoch, and S. Coen, Asymmetric balance in symmetry breaking Phys. Rev. Res. **2**, 023244 (2020).

[35] N. Moroney, L. Del Bino, S. Zhang, M. T. M. Woodley, L. Hill, T. Wildi, V. J. Wittwer, T. Südmeyer, G.-L. Oppo, M. R. Vanner *et al.*, A Kerr polarization controller Nat. Commun. **13**, 398 (2022).

[36] F. Copie, and M. T. M. Woodley, and L. Del Bino, J. M. Silver, S. Zhang, and P. Del'Haye, Interplay of Polarization and Time-Reversal Symmetry Breaking in Synchronously Pumped Ring Resonators Phys. Rev. Lett. **122**, 013905 (2019).